Title: PESCA: A scalable platform for the development of cell-type-specific viral drivers

One sentence summary: Highly paralleled functional evaluation of enhancer activity in single cells generates new cell-type-specific tools with broad medical and scientific applications.

Authors:

Sinisa Hrvatin[1, *], Christopher P. Tzeng[1], M. Aurel Nagy[1], Hume Stroud[1], Charalampia Koutsioumpa[1, 2], Oren F. Wilcox[1], Elena G. Assad[1], Jonathan Green[1], Christopher D. Harvey[1], Eric C. Griffith[1], Michael E. Greenberg[1, *]

Affiliations:

1. Department of Neurobiology, Harvard Medical School, Boston, Massachusetts, USA
2. BBS Program, Harvard Medical School, 220 Longwood Avenue, Boston, MA 02115, USA

*Co-corresponding authors:

Sinisa Hrvatin (sinisa_hrvatin@hms.harvard.edu),

Michael E. Greenberg (michael_greenberg@hms.harvard.edu)

Abstract:

Enhancers are the primary DNA regulatory elements that confer cell type specificity of gene expression. Recent studies characterizing individual enhancers have revealed their potential to direct heterologous gene expression in a highly cell-type-specific manner. However, it has not yet been possible to systematically identify and test the function of enhancers for each of the many cell types in an organism. We have developed PESCA, a scalable and generalizable method that leverages ATAC- and single-cell RNA-sequencing protocols, to characterize cell-type-specific enhancers that should enable genetic access and perturbation of gene function across mammalian cell types. Focusing on the highly heterogeneous mammalian cerebral cortex, we apply PESCA to find enhancers and generate viral reagents capable of accessing and manipulating a subset of somatostatin-expressing cortical interneurons with high specificity. This study demonstrates the utility of this platform for developing new cell-type-specific viral reagents, with significant implications for both basic and translational research.

Main text:

Introduction

Enhancers are DNA elements that regulate gene expression to produce the unique complement of proteins necessary to establish a specialized function for each cell type in an organism. Large scale efforts to build a definitive catalogue of cell types (*1–4*) based on their gene expression have recently successfully mapped epigenomic regulatory landscapes (*5–7*), enabling a mechanistic understanding of the underlying gene expression that is critical for cell-type-specific development, identity, and unique function. Importantly, characterization of individual enhancers has revealed their potential to direct highly cell-type-specific gene expression in both endogenous and heterologous contexts (*8–11*), making them ideal for developing tools to access, study, and manipulate virtually any mammalian cell type.

Despite recent success in cataloguing the gene expression profiles of distinct cell subpopulations in the nervous system, our limited ability to specifically access these subpopulations hinders the study of their function. For example, the mammalian cerebral cortex is composed of over one hundred cell types, most of which cannot be individually accessed using existing tools. Glutamatergic excitatory neuron cell types propagate electrical signals across neural circuits, whereas GABAergic inhibitory interneuron cell types play an essential role in cortical signal processing by modulating neuronal activity, balancing excitability, and gating information (*12–14*). Although relatively lower in abundance than excitatory neurons, interneurons are highly diverse; for example, somatostatin-expressing cortical interneurons comprise several anatomically, electrophysiologically, and molecularly defined cell types whose dysfunction is associated with neuropsychiatric and neurological disorders (*2*, *15*, *16*). Given the vast diversity of cell types in the brain, and the inability of our current tools to access most

70 neuronal cell types, enhancer-driven viral reagents have the potential to become the next
71 generation of cell-type-specific transgenic tools enabling facile, inexpensive, cross-species, and
72 targeted observation and functional study of neuronal cell-types and circuits.

73 Despite the potential of cell-type-specific enhancers to revolutionize neuroscience
74 research, cell-type-restricted gene regulatory elements (GREs) have not yet been systematically
75 identified. Moreover, functional evaluation of candidate GRE-driven viral vector expression
76 across all cell types in the tissue is currently laborious, expensive, and low-throughput, typically
77 relying on the production of individual viral vectors and the assessment of expression across a
78 limited number of cell types by *in situ* hybridization or immunofluorescence. The lack of a
79 generalizable platform for rapid identification and functional testing of cell-type-specific
80 enhancers is therefore a critical bottleneck impeding the generation of new viral reagents
81 required to elucidate the function of each cell type in a complex organism.

82 To address these issues, we merged the principles of massively parallel reporter assays
83 (MPRA) (*17–22*) with single-cell RNA sequencing (scRNA-seq) (*1–4*, *23–27*), and developed a
84 Paralleled Enhancer Single Cell Assay (PESCA) to identify and functionally assess the
85 *specificity* of hundreds of GREs across the full complement of cell types present in the brain. In
86 the PESCA protocol, the expression of a barcoded pool of AAV vectors harboring GREs is
87 analyzed by single-nucleus RNA sequencing (snRNA-seq) to evaluate the specificity of each
88 constituent GRE across tens of thousands of individual cells in the target tissue, through the use
89 of an orthogonal cell-indexed system of transcript barcoding (**Fig. 1a**).

90 We validated the efficacy of PESCA in the murine primary visual cortex by identifying
91 GREs that confine AAV expression to somatostatin (SST)-expressing interneurons and showed
92 that these vectors can be used to modulate neuronal activity selectively in SST neurons. We chose

93 to focus on SST neurons in the brain because this population is known to be diverse and to be
94 composed of several relatively rare subpopulations (*2*, *15*, *25*), and thus might serve as a good test
95 case. As described below, our findings highlight the utility of PESCA for identifying viral
96 constructs that drive gene expression selectively in a subset of neurons and establish PESCA as a
97 platform of broad interest to the research and gene therapy community, potentially enabling the
98 generation of cell-type-specific AAVs for virtually any cell type.
99

100 **Results**

101 **GRE selection and library construction**

102 To identify candidate SST interneuron-restricted gene regulatory elements (GREs), we
103 carried out comparative epigenetic profiling of the three largest classes of cortical interneurons:
104 somatostatin (SST)-, vasoactive intestinal polypeptide (VIP)- and parvalbumin (PV)-expressing
105 cells. To this end, we employed the recently developed isolation of nuclei tagged in specific cell
106 types (INTACT) (*5*) method to isolate purified chromatin from of each of these cell types from
107 the cerebral cortex of adult (6-10-week-old) mice. The assay for transposase-accessible
108 chromatin using sequencing (ATAC-Seq) (*7*), which identifies nucleosome-depleted gene
109 regulatory regions, was then used to identify genomic regions with enhanced accessibility (i.e.
110 peaks) in the SST (n = 57,932), PV (n = 61,108), and VIP (n = 79,124) chromatin samples (**Fig.
111 1b, c, Supplementary Fig 1, Methods)**. These datasets can be used as a resource to identify
112 putative gene regulatory elements as candidates for driving cell-type-specific gene expression for
113 the numerous subtypes of SST, PV or VIP-expressing intraneurons across diverse cortical
114 regions.

115 To enrich for GREs that could be useful reagents to study and manipulate interneurons
116 across mammalian species including humans, we started with an expanded list of 323,369
117 genomic coordinates (**Supplementary Table 1**) representing a union of cortical neuron ATAC-
118 seq accessible regions identified across dozens of experiments in our laboratory (**Methods**,
119 manuscript in preparation). We first filtered this initial set of 323,369 genomic coordinates to
120 exclude GREs with poor mammalian sequence conservation (**Methods**, **Supplementary Table**
121 **1, Supplementary Fig. 2**). The remaining 36,215 genomic regions were ranked by an
122 enrichment of ATAC-seq signal in the SST samples over PV/VIP (**Methods**), and the top 287
123 most enriched GREs were selected for functional screening to identify enhancers that drive gene
124 expression selectively in SST interneurons of the primary visual cortex (**Fig. 1d, Supplementary**
125 **Table 2**).
126 A PCR-based strategy was used to simultaneously amplify and barcode each GRE from
127 mouse genomic DNA (**Methods**). To minimize sequencing bias due to the choice of barcode
128 sequence, each GRE was paired with three unique barcode sequences. The resulting library of
129 861 GRE-barcode pairs was pooled and cloned into an AAV-based expression vector, with the
130 GRE element inserted 5' to a promoter driving a GFP expression cassette and the GRE-paired
131 barcode sequences inserted into the 3' untranslated region (UTR) of the GRE-driven transcript
132 (**Methods, Fig. 2a, Supplementary Fig. 3)**. This configuration was chosen to maximize the
133 retrieval of the barcode sequence during single-cell RNA sequencing, which primarily captures
134 the 3' end of transcripts. The human beta-globin promoter was chosen since it has previously
135 been used in conjunction with an enhancer to drive strong and specific expression in cortical
136 interneurons (*8*), although the modular cloning strategy is compatible with the use of other
137 promoters. The library was packaged into AAV9, which exhibits broad neural tropism and has

138 previously been used to drive payload expression in cortical neurons (*28*). The complexity of the
139 resulting rAAV-GRE library was then confirmed by next generation sequencing, detecting 802
140 of the 861 barcodes (93.2%), corresponding to 285 of the 287 GREs (99.3%) (**Fig. 2b**).
141

142 **PESCA screen identifies GREs highly enriched for SST$^+$ interneurons**

143 To quantify the expression of each rAAV-GRE vector across the full complement of cell types in
144 the mouse visual cortex, we used a modified single-nucleus RNA-Seq (snRNA-Seq) protocol to
145 first determine the cellular identity of each nucleus and then quantify the abundance of the GRE-
146 paired barcodes in the transcriptome of nuclei assigned to each cell type. Two adjacent injections
147 (800 nL each) of the pooled AAV library (1×10^{13} viral genomes/mL) were first administered to
148 the primary visual cortex (V1) of two 6-week-old C57BL/6 mice. Twelve days following
149 injection, the injected cortical regions were dissected and processed to generate a suspension of
150 nuclei for snRNA-Seq using the inDrops platform (*23*, *29*) (**Methods**). A total of 32,335 nuclei
151 were subsequently analyzed across the two animals, recovering an average of 866 unique non-
152 viral transcripts per nucleus, representing 610 unique genes (**Supplementary Fig. 4a, b**).
153 Since droplet-based high-throughput snRNA-Seq samples the nuclear transcriptome with
154 low sensitivity (*23*), viral-derived transcripts were initially detected in only 3.9% of sampled
155 nuclei. We therefore designed a modified PCR-based approach to enrich for barcode-containing
156 viral transcripts, which yielded deep coverage of AAV-derived transcripts with simultaneous
157 shallow coverage of the non-viral transcriptome. PCR enrichment increased the viral transcript
158 recovery 382-fold in the sampled nuclei, to an average of 15.6 unique viral transcripts, 6.0
159 unique GRE-barcodes, and 5.7 unique GREs per cell **(Fig. 2b, Supplementary Fig. 4c)**. Using
160 this modified protocol, viral transcripts were identified across 86% of cells (**Supplementary Fig.**

161 **4d**), with a high correlation ($r = 0.9$, $p < 2.2\times10^{-16}$) observed between the abundance of each
162 barcoded AAV in the library and the number of cells infected by that AAV (**Supplementary**
163 **Fig. 4f**), suggesting that GRE sequences did not alter viral tropism and that GRE-driven vectors
164 had broadly similar levels of expression. Only 0.3 ± .06% (mean, stdev) of viral reads did not
165 correspond to any of the known barcodes or could not be uniquely assigned to a barcode (within
166 2 mismatches), suggesting that this amplification strategy did not grossly change the composition
167 of the viral library.

168 Nuclei were classified into ten cell types using graph-based clustering and expression of
169 known marker genes **(Methods, Fig. 2c, d, Supplementary Fig. 5**). The average expression of
170 each viral-derived barcoded transcript was analyzed across all ten cell types, and an enrichment
171 score was calculated from the ratio of expression in *Sst*$^{+}$ nuclei compared to all *Sst*$^{-}$ nuclei. As
172 expected, sets of three barcodes associated with the same GRE showed highly statistically
173 correlated enrichment scores ($r = 0.52 \pm 0.05$, $p < 2.2\times10^{-16}$) (**Fig. 2e, f, Supplementary Fig. 6**),
174 which were significantly lower when barcodes were randomly shuffled (shuffled $r = 0.002 \pm$
175 0.06; Wilcox test between data and shuffled data, $p = 0.003$).

176 Having confirmed a robust, non-random correlation in enrichment scores among the three
177 barcodes associated with each GRE, we next computed a single expression value for each of the
178 287 viral drivers by aggregating expression data from three barcodes associated with the same
179 GRE, and carried out differential gene expression analysis between *Sst*$^{+}$ and *Sst*$^{-}$ cells for each
180 rAAV-GRE. Differential gene expression analysis between *Sst*$^{+}$ and *Sst*$^{-}$ cells for each rAAV-
181 GRE revealed a marked overall enrichment of viral-derived transcripts in the *Sst*$^{+}$ subpopulation
182 (**Supplementary Fig. 7a**). As expected, a high correlation was observed between GRE-specific

183 enrichment scores across two animals ($r = 0.54$, $p < 2.2\times10^{-16}$) (**Supplementary Fig. 7b**).
184 Among the 287 GREs tested, several viral drivers were identified that promoted highly specific
185 reporter expression in the *Sst*$^{+}$ subpopulation ($q < 0.01$, fold-change > 7, **Fig. 2h-j,**
186 **Supplementary Fig. 7c-e**). To assess how the abundance of each GRE in the library impacts our
187 ability to detect cell-type-specific expression, we analyzed the specificity of each GRE as a
188 function of the number of transcripts retrieved. We observed that highly abundant GRE-driven
189 transcripts were more likely to be significantly enriched in SST^{+} cells, suggesting that we may
190 not have had sufficient power to assess the cell-type-specificity of the less abundant GREs in the
191 library (**Supplementary Fig. 7f**). Consistent with this observation, computationally subsampling
192 the number viral transcripts across our most cell-type-specific GREs gradually reduced our
193 ability to statistically detect their enrichment in *Sst*$^{+}$ cells (**Supplementary Fig. 8)**. These
194 observations suggest that the expression of sparsely detected GRE-driven transcripts may not be
195 sufficient to allow evaluation of cell-type-specificity and that by increasing sequencing depth we
196 may be able to screen and evaluate a larger number of GREs.

197 ***In situ* characterization of rAAV-GRE reporter expression**

198 We next sought to validate the cell-type-specificity of the resulting hits using methods
199 that do not rely on single-cell sequencing-based approaches. To this end, we selected three of the
200 top five viral drivers (GRE12, GRE22, GRE44), as well as a control viral construct lacking the
201 GRE element (ΔGRE), for injection into V1 of adult transgenic Sst-Cre; Ai14 mice, in which
202 SST^{+} cells express the red fluorescent marker tdTomato (**Supplementary Table 3**).
203 Fluorescence analysis twelve days following injection with rAAV-[GRE12, GRE22 or GRE44]-
204 GFP revealed strong yet sparse GFP labeling centered around cortical layers IV and V (**Fig. 3a-**

205 **c)**. By contrast, the control rAAV-ΔGRE-GFP showed a strikingly different pattern of GFP
206 expression concentrated around the sites of injection, with expression in a larger number of cells
207 (**Fig. 3d**). Many rAAV-GRE12/22/44-GFP virally infected cells were SST-positive, as indicated
208 by the high degree of overlapping GFP and tdTomato expression: 90.7% ± 2.1% for rAAV-
209 GRE12-GFP (170 cells, 4 animals); 72.9 ± 4.2% for rAAV-GRE22-GFP (1164 cells, 3 animals),
210 and 95.8 ± 0.6% for rAAV-GRE44-GFP (759 cells, 4 animals). (**Fig. 3e, f, Supplementary Fig.**
211 **9**). By contrast, we observed that 27.2 ± 1.9% of GFP^+ cells also expressed tdTomato following
212 rAAV-ΔGRE-GFP infection (2066 cells, 3 animals, **Fig. 3e, f**). Although the 27.2% overlap
213 between rAAV-ΔGRE-GFP expression and SST^+ cells suggests that our vector has some
214 baseline preference for SST^+ interneurons, the insertion of GRE12, GRE22 and GRE44 serves to
215 effectively restrict AAV payload expression to SST^+ interneurons. To show that not all the
216 enhancers exhibited strong SST-specificity using our viral vector, we cloned the mDlx5/6
217 enhancer whose expression was restricted to a broader population of inhibitory neurons (*8*). We
218 injected the rAAV2/9-mDlx5/6-GFP vector and observed that 42.9 % of GFP^+ cells were also
219 positive for tdTomato (1977 cells, 3 animals, **Supplementary Fig. 10**). It is notable that the
220 GREs seemingly not only promote expression in SST^+ cells but also greatly reduce background
221 expression in SST negative cells, indicating both enhancer and repressor functionality.
222 Consistent with this hypothesis, the incorporation of GRE12, GRE22 and GRE44 into the rAAV
223 both increased the number of SST^+ GFP^+ cells (1.7-2-fold) and dramatically (3-32-fold)
224 decreased the number of SST^- cells that expressed GFP (**Fig. 3g, Supplementary Fig. 11**). To
225 further investigate the specificity of our viral drivers among cortical interneuron cell types we

226 injected each construct into Vip-Cre; Ai14$^+$ mice in which all VIP$^+$ cells express tdTomato, or

227 used fluorescence antibody staining to label PV-expressing cells (**Supplementary Fig. 12)**.

228 Fluorescent signal analysis indicated the percentage of GFP$^+$ cells that were either VIP$^+$ or PV$^+$

229 (rAAV-SST12-GFP$^+$ [2.6 ± 2.6%], rAAV-GRE22-GFP$^+$ [3.5 ± 2.0%] and rAAV-GRE44-GFP$^+$

230 [6.0 ± 2.7%], **Fig. 3h**). These findings confirm that among major interneuron cell classes, all

231 three GRE-driven vectors are highly SST-specific.

232 Because at least five subtypes of cortical SST$^+$ interneurons have previously been

233 identified based on the laminar distribution of their cell bodies and projections (*15*, *30*), we

234 investigated the laminar distribution of GFP-expressing cells for the three Sst-enriched viral

235 drivers. Intriguingly, the majority of rAAV-GRE12-GFP$^+$ and rAAV-GRE44-GFP$^+$ SST$^+$ cells

236 were found to reside in layers IV and V, which was distinct from the distribution observed for

237 the full SST$^+$ cell population in visual cortex ($p = 1.3\times10^{-6}$, $p < 2.2\times10^{-16}$, respectively, Mann-

238 Whitney *U* test, two-tailed, **Fig. 3i, Supplementary Fig. 13**). By contrast, rAAV-ΔGRE-GFP

239 labeled SST$^+$ cells as well as other neuronal subtypes across all layers, suggesting that the

240 confined labeling of rAAV-GRE12-GFP and rAAV-GRE44-GFP to layer IV and V was likely

241 due to restricted gene expression and not restricted viral tropism. These findings suggest that

242 PESCA may support the isolation of viral drivers capable of discriminating between fine-grained

243 cell-types within a given interneuron cell class.

244

245 **Electrophysiological characterization of rAAV-GRE-GFP-expressing SST subtypes**

246 In addition to variability in laminar distribution, different electrophysiological
247 phenotypes have also been observed in cortical SST interneurons (*31*, *32*). To determine
248 whether AAV-GRE reporters can be used to distinguish electrophysiologically distinct SST
249 subtypes, we injected our most cell-type-restricted construct rAAV-GRE44-GFP into the visual
250 cortex of adult Sst-Cre; Ai14 mice and obtained whole-cell current-clamp recordings from
251 double GFP- and tdTomato-positive neurons (rAAV-GRE44-GFP$^+$), as well as immediately
252 nearby tdTomato-positive but GFP-negative cells (rAAV-GRE44-GFP$^-$).

253 Our recordings indicate that both rAAV-GRE44-GFP$^+$ and rAAV-GRE44-GFP$^-$ SST$^+$
254 neurons display the properties of adapting SST interneurons with high input resistances and
255 features consistent with those previously reported for deep layer cortical SST neurons(*31*, *33*)
256 (**Fig. 4a, b**). However, rAAV-GRE44-GFP$^+$ SST neurons are distinct with respect to several
257 electrophysiological parameters. The action potentials of rAAV-GRE44-GFP$^+$ SST neurons are
258 significantly broader than those of rAAV-GRE44-GFP$^-$ SST neurons (**Fig. 4c, d**), perhaps due to
259 differences in expression of specific channels in these subgroups of SST neurons, such as
260 voltage-activated potassium channels, and BK calcium-activated potassium channels(*34*, *35*).
261 Furthermore, rAAV-GRE44-GFP$^+$ SST neurons have a lower rheobase, and fire action potentials
262 with a slower rising phase, and at lower maximal frequencies compared to rAAV-GRE44-GFP$^-$
263 SST neurons **(Fig. 4a, d, Supplementary Table 4)**. Although we cannot confirm that GRE44
264 expression is restricted to a specific transcriptionally defined subtype of SST interneurons, our
265 electrophysiology experiments further emphasize the potential of PESCA to target functionally
266 distinct subgroups of previously defined interneuron types.

267

268 **Modulation of neuronal activity with rAAV-GREs**

269 Finally, we evaluated whether the identified SST^+ neuron-restricted viral drivers support

270 sufficiently high and persistent levels of payload expression to effectively modulate SST^+ cell

271 physiology. Designer receptors exclusively activated by designer drugs (DREADDs) are a

272 commonly employed viral payload used to dynamically regulate neuronal activity in response to

273 the synthetic ligand clozapine-N-oxide (CNO)(*36*). We therefore injected the visual cortex of

274 adult wild-type mice (6-8-week-old) with rAAV-GRE12-Gq-DREADD-tdTomato, a construct in

275 which GRE12 drives the expression of an activating DREADD as well as tdTomato. GRE12 was

276 chosen for this assay as it drives the weakest expression of the three evaluated GREs (**Fig. 2e)**

277 and thus, if it effectively drives DREADD expression, the other GREs might be expected to as

278 well. We obtained electrophysiological recordings from $tdTomato^+$ cells of acute cortical slices

279 in a whole-cell, current-clamp configuration two weeks post-injection. All $tdTomato^+$ cells

280 showed striking sensitivity to CNO, as indicated by significantly increased firing rates in

281 response to depolarizing current steps and depolarized resting membrane potentials (**Fig. 4e-g**).

282 To ensure that increases in firing rate upon CNO application were specific to infected SST^+

283 neurons, we obtained recordings from nearby uninfected pyramidal neurons that were identified

284 by morphology and found that there was no statistically significant increase in firing rate upon

285 CNO application (**Fig. 4h-j**). These data demonstrate the ability of GRE-driven SST^+ neuron-

286 specific reagents to robustly and specifically modulate the activity of SST^+ cells in non-

287 transgenic animals.

288 **Discussion**

289 The PESCA platform extends previous paralleled reporter assays (*17–22*) carried out
290 using bulk tissue or sorted cells by including a single-cell RNA-seq-based readout (*1–4*, *23–27*)
291 to evaluate the cell-type-specificity of gene expression. This represents a significant
292 advancement over current approaches to viral vector design, as it enables the rapid *in vivo*
293 screening of hundreds of GREs for enhanced cell-type-specificity without needing transgenic
294 tools to evaluate their specificity. In this study, we applied PESCA to identify enhancer elements
295 that robustly and specifically drive gene expression in a rare SST^+ population of GABAergic
296 interneurons in the mouse central nervous system, although further work is needed to identify
297 which specific molecular subtypes of SST interneurons are targeted. Since the vectors used in
298 this PESCA screen in the absence of GREs show broad expression in the murine V1, the GREs
299 we identified likely function to both enhance and restrict viral expression by a mechanism that
300 remains to be explored.

301 In the future, several factors should be considered to facilitate the further optimization of
302 the PESCA methodology for the development of cell-type-specific vectors. The selection of
303 candidate GREs for screening will benefit from the systematic profiling of additional cell types
304 by traditional or single-cell ATAC-Seq methods. In this regard, consideration of a published
305 ATAC-Seq dataset from excitatory neurons(*5*) could have served to refine our starting GRE set
306 by excluding approximately half of the screened GREs from our initial pool. This is particularly
307 relevant insofar as the ability to assess the GRE library depends on the number of cells
308 sequenced from the target and non-target populations and the sequencing depth, as the coverage
309 of each GRE will be inversely proportional to the number of GREs screened. In the screen

310 described here, we estimate having sufficient power to assess approximately 2/3 of the 287
311 GREs at the reported sequencing depth (**Supplementary Fig. 7**).
312 If a robust method of specifically isolating RNA from the target cell population is
313 available, screening the PESCA library by sequencing pooled RNA from all target versus all
314 non-target cells would provide less expensive and potentially more scalable approach. However,
315 by averaging across multiple non-target cell types, such an approach could be confounded by the
316 presence of rare, highly expressing non-target cells. Similarly, among single-cell methods,
317 single-nucleus RNA-seq is technically simpler and can be used on frozen tissue but recovers
318 fewer transcripts per cell compared to single-cell RNA-seq.
319 Finally, once candidate PESCA hits have been identified, we suggest evaluating several
320 in follow-up assays at multiple titers to identify which among these hits have the desired
321 intensity and specificity of protein expression. In this regard, the snRNA-seq PESCA screen
322 identified GRE12, GRE22 and GRE44 as, respectively, 8.3-, 9.1- and 7.2-fold more highly
323 expressed in SST^+ compared to SST^- cells, whereas these GREs showed distinct specificity for
324 SST^+ cells (91%, 73% and 96% respectively, **Fig. 3f**) when evaluated at the protein level, a
325 finding which could be attributed to a variety of factors.
326 Given current evidence that the mechanisms of gene regulatory element function are
327 conserved across tissues and species, it is likely that PESCA can be readily applied to other
328 neuronal or non-neuronal cells types, diverse model organisms, tissues, and viral types.
329 Moreover, PESCA is not limited to GRE screening; the method can be easily adapted to assess
330 the cell-type-specificity of viral capsid variants or other mutable aspects of viral design. Indeed,
331 the PESCA library cloning strategy is largely vector- and capsid-independent, allowing for the
332 use of different promoters or serotypes. Our choice of capsid and promoter was driven by

333 previous work using AAV9 and the minimal beta-globin promoter to drive expression in cortical
334 interneurons (*8*), however, different capsids or promoter may be preferred for targeting other cell
335 types.
336 In conclusion, our study addresses the urgent practical need for new tools to access, study, and
337 manipulate specific cell types across complex tissues, organ systems, and animal models by
338 providing a screening platform that can be used to rapidly supply such tools as needed.
339 Moreover, as the promise of gene therapy to treat and cure a broad range of diseases is being
340 realized, PESCA has the potential to pave the way for a new generation of targeted gene therapy
341 vehicles for diseases with cell-type-specific etiologies, such as congenital blindness, deafness,
342 cystic fibrosis, and spinal muscular atrophy.

343 **Figures and figure legends**

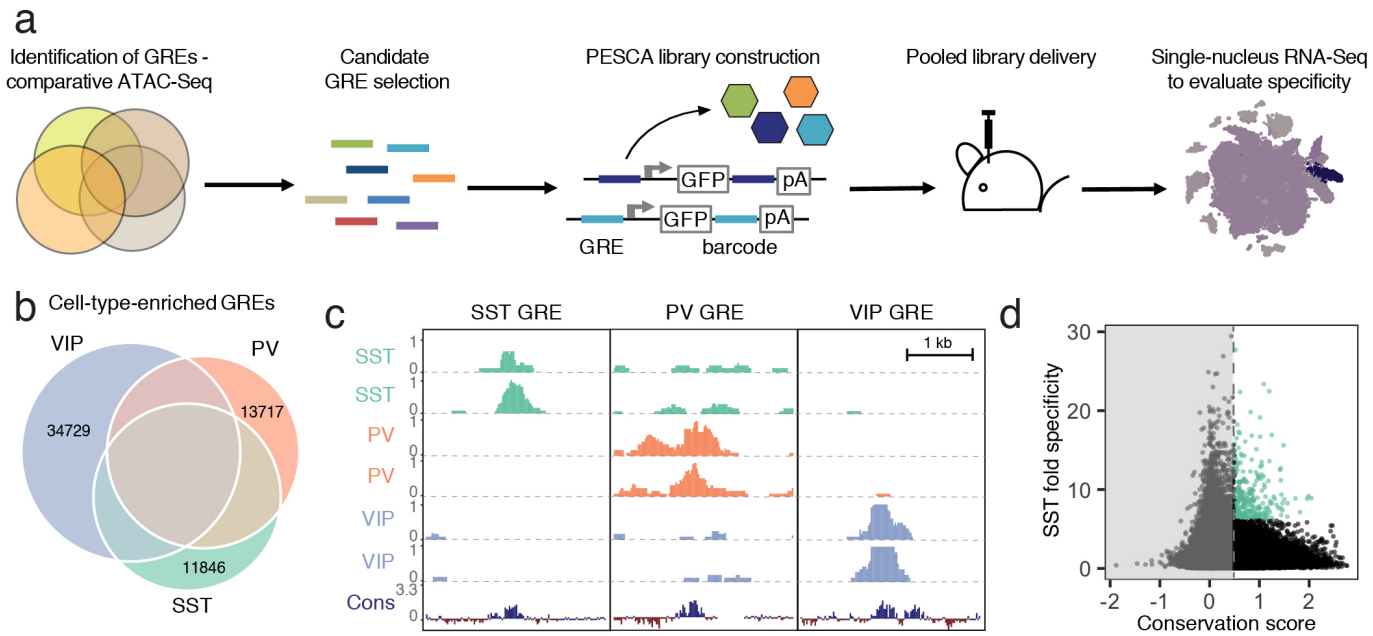

344 **Figure 1 – Experimental strategy and GRE selection**

345 (**a**) Paralleled Enhancer Single Cell Assay (PESCA). Comparative ATAC-Seq is used to
346 identify candidate GREs. A library of gene regulatory elements (GREs) is inserted upstream of a
347 minimal promoter-driven GFP. The viral barcode sequence is inserted in the 3'UTR, and the
348 vector packaged into rAAVs. Following *en masse* injection of the rAAV library, the specificity
349 of the constituent GREs for various cell types *in vivo* is determined by single-nucleus RNA
350 sequencing, measuring expression of the barcoded transcripts in tens of thousands of individual
351 cells in the target tissue. Finally, bioinformatic analysis determines the most cell-type-specific
352 barcode-associated rAAV-GRE-GFP constructs. pA = polyA tail.

353 (**b**) Area-proportional Venn diagram of the number of putative GREs identified by
354 ATAC-Seq of purified PV, SST, and VIP nuclei. Overlapping areas indicate shared putative
355 GREs. Non-overlapping areas represent GREs that are unique to a single cell type.

356 (**c**) Representative ATAC-seq genome browser traces of a putative GRE enriched in SST-
357 , PV-, or VIP-interneurons (normalized counts per location). Sequence conservation across the
358 Placental mammalian clade is also shown.
359 (**d**) Putative GREs (n = 323,369) are plotted based on average sequence conservation
360 (phyloP, 60 placental mammals) and SST-specificity (ratio of the average ATAC-Seq signal
361 intensity between SST samples and non-SST samples). Dashed vertical line indicates the
362 minimal conservation value cutoff (0.5). Green coloring indicates the 287 most SST-specific
363 GREs selected for PESCA screening.

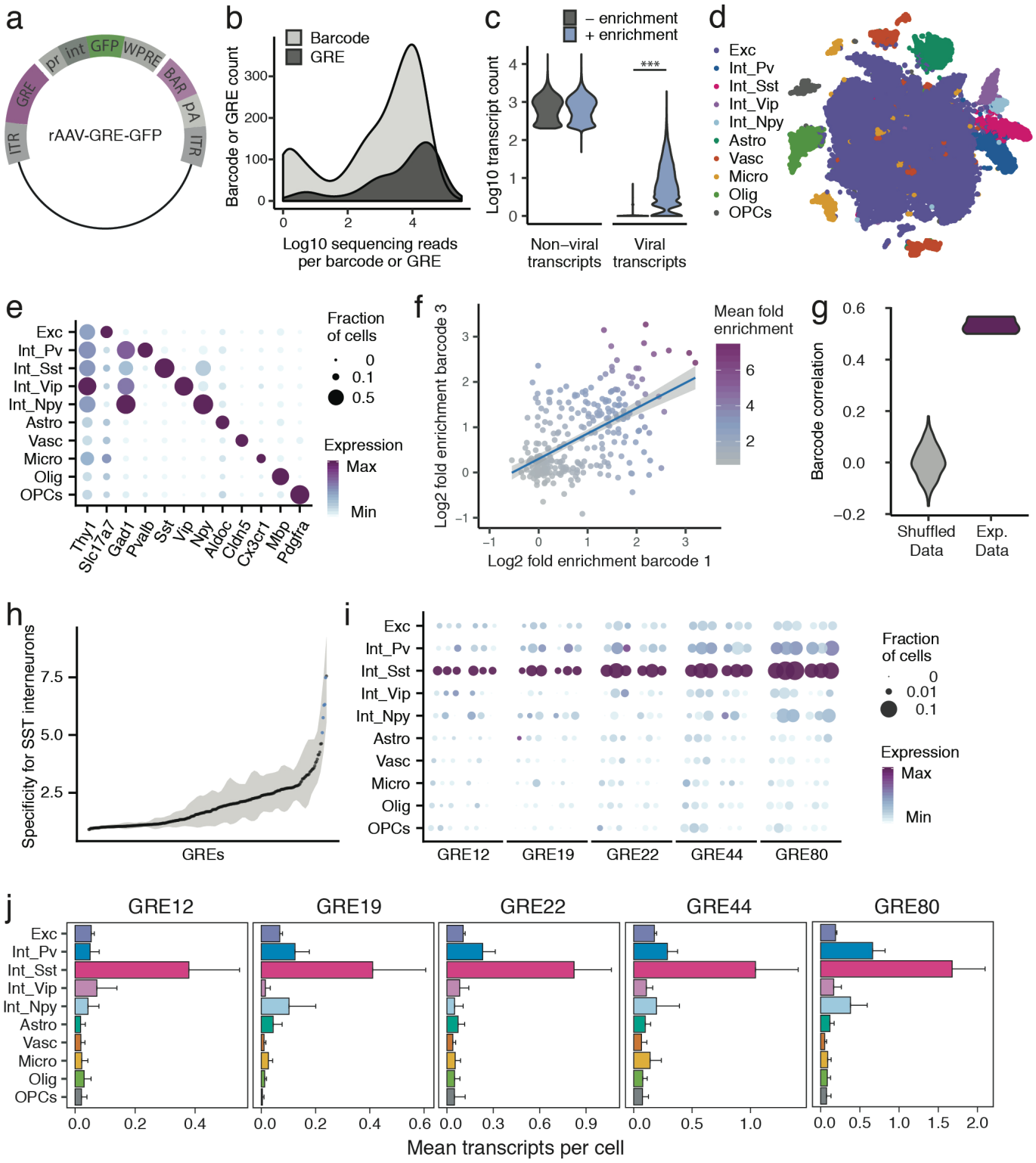

364 **Figure 2 – PESCA screen identifies GREs highly enriched for SST^{+} interneurons**

365 (**a**) PESCA library plasmid map. ITR, inverted terminal repeats; GRE, gene regulatory
366 element; pr, HBB minimal promoter; int, intron; GFP, green fluorescent protein; WPRE,
367 Woodchuck Hepatitis Virus post-transcriptional regulatory element; BAR, 10-mer sequence
368 barcode associated with each GRE; pA, polyadenylation signal.
369 (**b**) Library complexity plotted as distribution of the abundance of the 861 barcodes and
370 287 GREs in the AAV library. Barcodes and GREs were binned by number of sequencing reads
371 attributed to each barcode or GRE within the library.
372 (**c**) Transcript count per nucleus (n = 32,335 nuclei). Sequencing libraries were prepared
373 with or without PCR-enrichment for viral transcripts. PCR enrichment resulted in a 382-fold
374 increase in the number of recovered viral transcripts (p = 0, Mann-Whitney U-test, two-sided) to
375 an average of 15.6 unique viral transcripts per nucleus. Displayed as Log10(Count+1).
376 (**d**) t-SNE plot of 32,335 nuclei from V1 cortex of two animals**.** Colors denote main cell
377 types: Exc (Excitatory neurons), Pv (PV Interneurons), Sst (SST Interneurons), Vip (VIP
378 interneurons), Npy (NPY Interneurons), Astro (Astrocytes), Vasc (Vascular-associated cells),
379 Micro (Microglia), Olig (Oligodendrocytes), OPCs (Oligodendrocyte precursor cells).
380 (**e**) Marker gene expression across cell types. Color denotes mean expression across all
381 nuclei normalized to the highest mean across cell types. Size represents the fraction of nuclei in
382 which the marker gene was detected.
383 (**f**) Dot plot with each dot representing one GRE (n = 287). The values on each axis
384 represent the Log2 SST fold-enrichment calculated for each GRE based on two of the three
385 barcodes paired with that GRE - barcode 1 on the x-axis, and barcode 3 on the y-axis. Blue line
386 indicates linear fit with 95% confidence intervals (shaded) ($r = 0.55$, $p < 2.2\times10^{-16}$, Pearson's
387 correlation). Color gradient indicates the average enrichment between the two barcodes.

388 (**g**) Pairwise Pearson correlation between the enrichment values calculated from three sets
389 of barcodes associated with 287 GREs for experimental data (Exp. Data, $r = 0.52 \pm 0.05$, $p <$
390 2.2×10^{-16}, Pearson's correlation) and after random shuffling of enrichment values (Shuffled Data,
391 $r = 0 \pm 0.06$).
392 (**h**) GREs ranked by average barcode expression specificity for SST interneurons across
393 three barcodes. Shading indicates the minimal and maximal specificity calculated by analyzing
394 each of the three barcodes associated with a GRE. Blue indicates the five top hits that also passed
395 a statistical test for SST interneuron enrichment (FDR-corrected $q < 0.01$).
396 (**i**) Expression of the top five hits: GRE12, GRE19, GRE22, GRE44, GRE80. For each
397 GRE, expression values are split into two animals, and, for each animal, into the three barcodes
398 associated with that GRE. Color denotes mean expression across all nuclei normalized to the
399 highest mean across cell types. Size represents the fraction of nuclei in which the marker gene
400 was detected.
401 (**j**) Mean expression of GRE12, GRE19, GRE22, GRE44, and GRE80 across cell types.
402 Error bars, s.e.m.
403

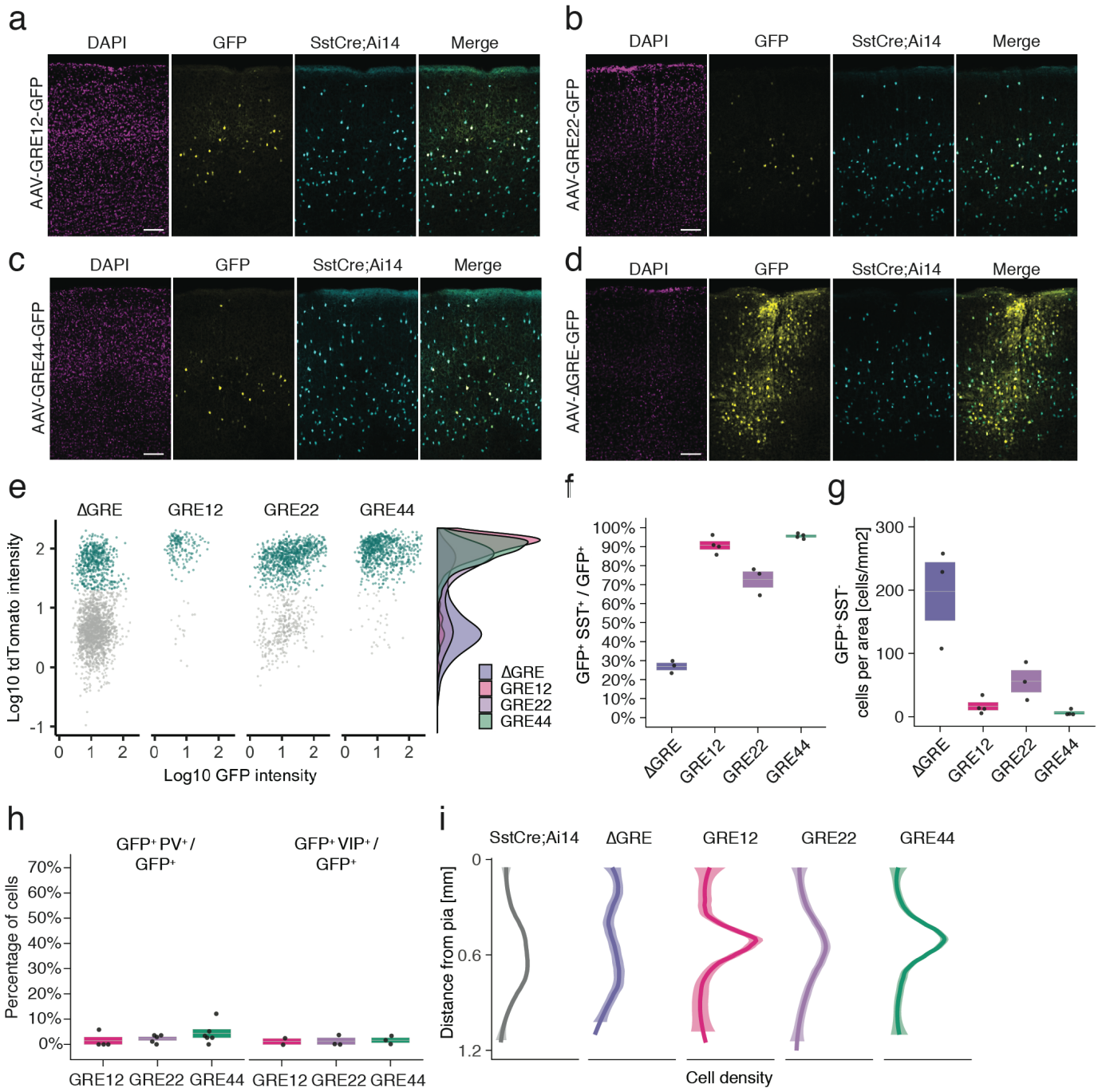

Figure 3 – *In situ* characterization of rAAV-GRE reporter expression

(**a-d**) Fluorescent images from adult Sst-Cre; Ai14 mouse visual cortex twelve days following injection with rAAV-GRE-GFP as indicated. Scale bars 100 µm.

407 (**e**) Identification of rAAV-GRE-GFP$^+$ cells that express tdTomato (SST$^+$). Each dot

408 represents a GFP$^+$ cell (n = 2066, 172, 1164, and 765, for AAV-[ΔGRE, GRE12, GRE22,

409 GRE44]-GFP, respectively). Cyan indicates tdTomato$^+$ (SST$^+$) cells. Distribution of cell

410 frequency across tdTomato intensity is plotted on the right for each construct.

411 (**f**) Quantification of the fraction of GFP$^+$ cells that are SST$^+$. Each dot represents one

412 animal. Box plot represents mean ± standard error of the mean (s.e.m). Values are 27.2 ± 1.9%,

413 90.7 ± 2.1, 72.9 ± 4.2%, and 95.8 ± 0.6% for AAV-[ΔGRE, GRE12, GRE22, GRE44]-GFP,

414 respectively.

415 (**g**) Quantification of the number of GFP$^+$ SST$^-$ cells normalized for area of infection.

416 Each dot represents one animal. Box plot represents mean ± standard error of the mean (s.e.m).

417 Values are 198.0 ± 46.0, 16.4 ± 6.2, 56.0 ± 17.3 and 6.1± 2.1 cells/mm^2 for AAV-[ΔGRE,

418 GRE12, GRE22, GRE44]-GFP, respectively.

419 (**h**) Quantification of the fraction of GFP$^+$ cells that are PV$^+$ or VIP$^+$. Box plot represents

420 mean ± standard error of the mean (s.e.m). Fraction of AAV-GRE-GFP$^+$ cells that are PV$^+$ is 1.4

421 ± 1.4%, 2.2 ± 0.7, and 4.3 ± 1.7% for AAV-[GRE12, GRE22, GRE44]-GFP, respectively.

422 Similarly, the fraction of AAV-GRE-GFP$^+$ cells that are VIP$^+$ is 1.2 ± 1.2%, 1.3 ± 1.3%, and 1.7

423 ± 1.0% for AAV-[GRE12, GRE22, GRE44]-GFP$^+$ cells, respectively.

424 (**i**) Distribution of the location of GFP-expressing cells as function of distance from the

425 pia. Gray represents SST$^+$ cells (n = 2648); Colored lines represents GFP$^+$ SST$^+$ cells (n = 2066,

426 172, 1164, and 765, respectively, for AAV-[ΔGRE, GRE12, GRE22, GRE44]-GFP). Shading

427 represents the 95% confidence interval.

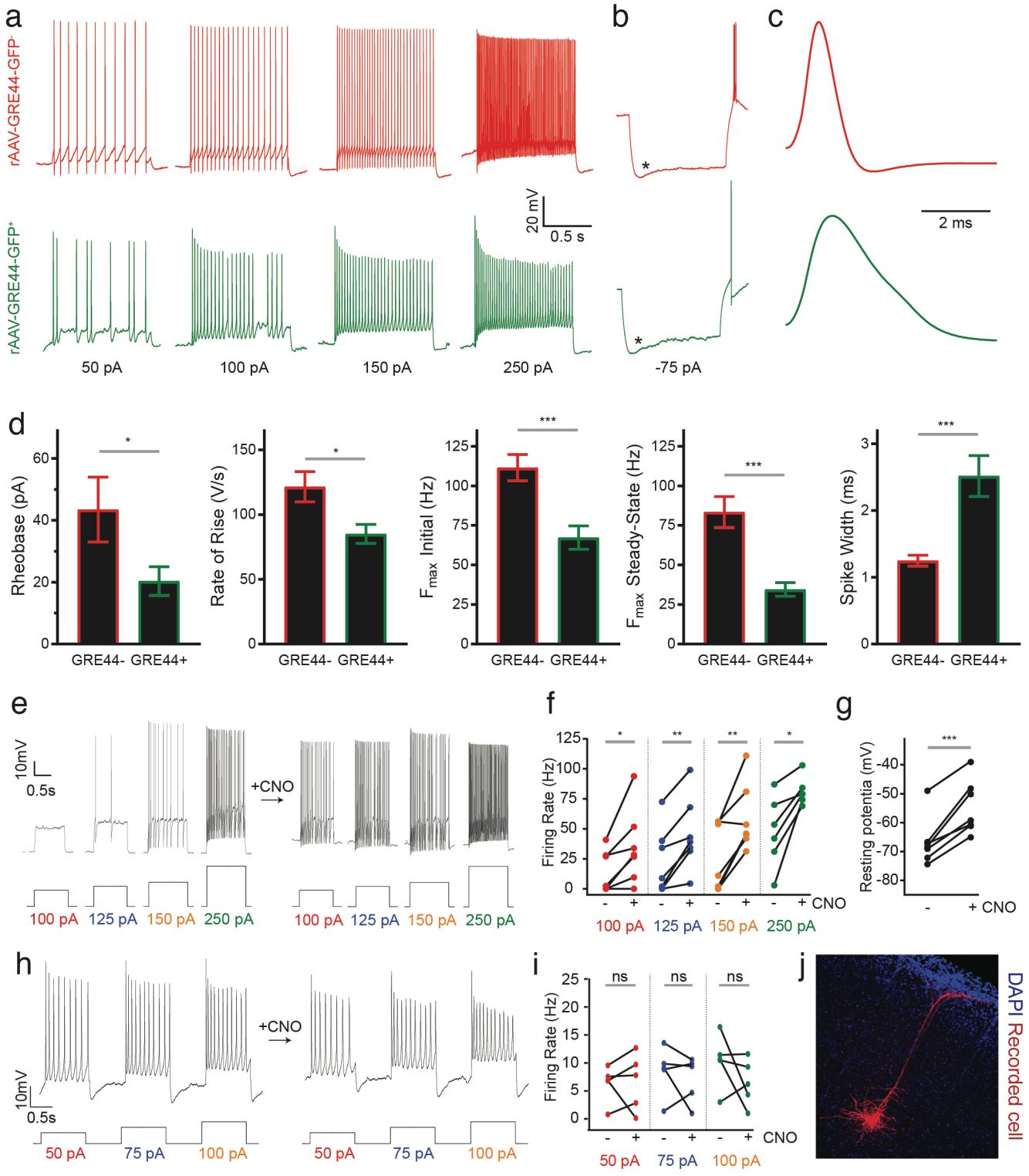

428 **Figure 4 – Electrophysiology of neurons expressing an rAAV-GRE-driven reporter and**

429 **modulation of neuronal activity with rAAV-GREs**

430 (**a**) Representative current-clamp recordings from SST neurons in the visual cortex of
431 Sst-Cre; Ai14 mice injected with rAAV-GRE44-GFP. *Top*: Representative traces from a cortical
432 SST neuron with Cre-dependent expression of red fluorescent protein (RFP), in response to 1000
433 ms depolarizing current injections as indicated in black ("GRE44-"). *Bottom*: Traces from a
434 RFP^+ SST neuron with GRE44-driven expression of GFP ("$GRE44^+$"). GRE44- SST neurons
435 were only recorded in the immediate vicinity of $GRE44^+$ SST neurons.

436 (**b**) Recordings from $GRE44^+$ and $GRE44^-$ neurons in response to hyperpolarizing, 1000
437 ms currents. Asterisks indicate the sag likely due to the hyperpolarization-activated current I_h.
438 Rebound action potentials following recovery from hyperpolarization, likely due to low-
439 threshold calcium spikes mediated by T-type calcium channels, were also present in cells of both
440 groups. Same scale as (a).

441 (**c**) Broader action potentials in $GRE44^+$ SST neurons (bottom) compared to $GRE44^-$
442 SST neurons (top). Same vertical scale as (a) and (b).

443 (**d**) Electrophysiological properties that differ between $GRE44^+$ (n=16 cells from 5 mice)
444 and $GRE44^-$ (n=16 cells from 4 mice) SST neurons, including rheobase (minimal amount of
445 current necessary to elicit a spike), maximal rate of rise during the depolarizing phase of the
446 action potential, the initial and steady state firing frequencies (both measured at the maximal
447 current step before spike inactivation), and spike width (measured as the width at half-maximal
448 spike amplitude). * $p < 0.05$; *** $p < 0.001$, paired t-test, two-tailed.

449 (**e**) Representative current-clamp recordings from AAV-GRE12-Gq-$tdTomato^+$ cells
450 before and during CNO application.

451 (**f**) Increased firing rates of AAV-GRE12-Gq-tdTomato^{+} cells evoked by depolarizing

452 current injections upon bath application of CNO (3 animals, 6-7 cells). * $p < 0.05$; ** $p < 0.01$,

453 paired t-test, two-tailed.

454 (**g**) Robust depolarization of AAV-GRE12-Gq-tdTomato^{+} cells upon bath application of

455 CNO (3 animals, 6-7 cells). *** $p < 0.001$, paired t-test, two-tailed.

456 (**h**) Representative recordings from nearby uninfected pyramidal neurons in the visual

457 cortex of mice that were injected with AAV-GRE-12-Gq-tdTomato^{+}, before (top) and during

458 CNO application (bottom).

459 (**i**) Firing rates of pyramidal neurons during CNO application remain unchanged (3

460 animals, 5 cells). ns, $p > 0.05$, paired t-test, two-tailed.

461 (**j**) Representative image of nearby uninfected pyramidal neuron that was recorded from

462

463

464

465

466

467

468

469

470

471

472

Acknowledgements

We thank D. Tom for help with image analysis, Dr. W. Renthal and members of the Greenberg lab for discussions, the HMS Single Cell Core for single-nucleus RNA-seq sample processing, Boston Children's Hospital Viral Core for AAV packaging, Dr. B. Bean for feedback on electrophysiology, and the Harvard NeuroDiscovery Center Enhanced Neuroimaging Core for imaging and image analysis. This work was supported by the National Institute of Health BRAIN Initiative grant R01 MH114081-01, NIH grant T32GM007753 to M.A.N. and NIH Training in the Molecular Biology of Neurodegeneration grant 5T32AG000222-23 to S.H.

Author Contributions

S.H. conceived the study and designed the experiments. H.S. performed ATAC-Seq. M.A.N. aligned and called peaks for ATAC-seq data; S.H. calculated ATAC-seq enrichment and selected elements for screen. S.H. cloned the library and performed the PESCA screen. M.A.N. mapped snRNA-seq data and quantified viral barcodes. S.H. analyzed snRNA-seq data. S.H., C.K. and O.F.W. cloned individual viral constructs. O.F.W. performed stereotactic injections and tissue sectioning. S.H. and E.G.A. performed imaging and image analysis. C.P.T. performed and analyzed electrophysiology recordings. J.G., C.D.G., E.C.G. and M.E.G. advised on the study. S.H., C.P.T., M.A.N, E.C.G. and M.E.G. wrote the manuscript.

Competing Financial Interests

The authors declare no competing financial interests.

496

497

498 **Correspondence**

499 Correspondence and requests for materials should be addressed to S.H.

500 (sinisa_hrvatin@hms.harvard.edu) or M.E.G. (michael_greenberg@hms.harvard.edu).

501

502 **References**

503 1. A. Zeisel, A. B. Muñoz-Manchado, S. Codeluppi, P. Lönnerberg, G. L. Manno, A. Juréus, S.
504 Marques, H. Munguba, L. He, C. Betsholtz, C. Rolny, G. Castelo-Branco, J. Hjerling-
505 Leffler, S. Linnarsson, Cell types in the mouse cortex and hippocampus revealed by single-
506 cell RNA-seq. *Science*. **347**, 1138–1142 (2015).

507 2. B. Tasic, Z. Yao, L. T. Graybuck, K. A. Smith, T. N. Nguyen, D. Bertagnolli, J. Goldy, E.
508 Garren, M. N. Economo, S. Viswanathan, O. Penn, T. Bakken, V. Menon, J. Miller, O.
509 Fong, K. E. Hirokawa, K. Lathia, C. Rimorin, M. Tieu, R. Larsen, T. Casper, E. Barkan, M.
510 Kroll, S. Parry, N. V. Shapovalova, D. Hirschstein, J. Pendergraft, H. A. Sullivan, T. K.
511 Kim, A. Szafer, N. Dee, P. Groblewski, I. Wickersham, A. Cetin, J. A. Harris, B. P. Levi, S.
512 M. Sunkin, L. Madisen, T. L. Daigle, L. Looger, A. Bernard, J. Phillips, E. Lein, M.
513 Hawrylycz, K. Svoboda, A. R. Jones, C. Koch, H. Zeng, Shared and distinct transcriptomic
514 cell types across neocortical areas. *Nature*. **563**, 72–78 (2018).

515 3. J. Cao, J. S. Packer, V. Ramani, D. A. Cusanovich, C. Huynh, R. Daza, X. Qiu, C. Lee, S. N.
516 Furlan, F. J. Steemers, A. Adey, R. H. Waterston, C. Trapnell, J. Shendure, Comprehensive
517 single-cell transcriptional profiling of a multicellular organism. *Science*. **357**, 661–667
518 (2017).

519 4. A. B. Rosenberg, C. M. Roco, R. A. Muscat, A. Kuchina, P. Sample, Z. Yao, L. T.
520 Graybuck, D. J. Peeler, S. Mukherjee, W. Chen, S. H. Pun, D. L. Sellers, B. Tasic, G.
521 Seelig, Single-cell profiling of the developing mouse brain and spinal cord with split-pool
522 barcoding. *Science*. **360**, 176–182 (2018).

523 5. A. Mo, E. A. Mukamel, F. P. Davis, C. Luo, G. L. Henry, S. Picard, M. A. Urich, J. R. Nery,
524 T. J. Sejnowski, R. Lister, S. R. Eddy, J. R. Ecker, J. Nathans, Epigenomic Signatures of
525 Neuronal Diversity in the Mammalian Brain. *Neuron*. **86**, 1369–1384 (2015).

526 6. D. A. Cusanovich, R. Daza, A. Adey, H. A. Pliner, L. Christiansen, K. L. Gunderson, F. J.
527 Steemers, C. Trapnell, J. Shendure, Multiplex single-cell profiling of chromatin
528 accessibility by combinatorial cellular indexing. *Science*. **348**, 910–914 (2015).

529 7. J. D. Buenrostro, B. Wu, U. M. Litzenburger, D. Ruff, M. L. Gonzales, M. P. Snyder, H. Y.
530 Chang, W. J. Greenleaf, Single-cell chromatin accessibility reveals principles of regulatory
531 variation. *Nature*. **523**, 486–490 (2015).

532 8. J. Dimidschstein, Q. Chen, R. Tremblay, S. L. Rogers, G.-A. Saldi, L. Guo, Q. Xu, R. Liu, C.
533 Lu, J. Chu, J. S. Grimley, A.-R. Krostag, A. Kaykas, M. C. Avery, M. S. Rashid, M. Baek,
534 A. L. Jacob, G. B. Smith, D. E. Wilson, G. Kosche, I. Kruglikov, T. Rusielewicz, V. C.
535 Kotak, T. M. Mowery, S. A. Anderson, E. M. Callaway, J. S. Dasen, D. Fitzpatrick, V.
536 Fossati, M. A. Long, S. Noggle, J. H. Reynolds, D. H. Sanes, B. Rudy, G. Feng, G. Fishell,
537 A viral strategy for targeting and manipulating interneurons across vertebrate species. *Nat.*
538 *Neurosci.* **19**, 1743–1749 (2016).

539 9. J. Juettner, A. Szabo, B. Gross-Scherf, R. Morikawa, S. Rompani, M. Teixeira, P. Hantz, T.
540 Szikra, F. Esposti, C. Cowan, A. Bharioke, C. Patino, O. Keles, C. Roth, A. Kusnyerik, N.
541 Gerber-Hollbach, T. Azoulay, D. Hartl, A. Krebs, D. Schuebeler, R. Hajdu, A. Lukats, J.
542 Nemeth, Z. Nagy, K.-C. Wu, R.-H. Wu, L. Xiang, X.-L. Fang, Z.-B. Jin, D. Goldblum, P.
543 Hasler, H. Scholl, J. Krol, B. Roska, Targeting neuronal and glial cell types with synthetic
544 promoter AAVs in mice, non-human primates, and humans. *bioRxiv*, 434720 (2018).

545 10. L. T. Graybuck, A. Sedeño-Cortés, T. N. Nguyen, M. Walker, E. Szelenyi, G. Lenz, L.
546 Sieverts, T. K. Kim, E. Garren, B. Kalmbach, S. Yao, M. Mortrud, J. Mich, J. Goldy, K. A.
547 Smith, N. Dee, Z. Yao, A. Cetin, B. P. Levi, E. Lein, J. Ting, H. Zeng, T. Daigle, B. Tasic,
548 Prospective, brain-wide labeling of neuronal subclasses with enhancer-driven AAVs.
549 *bioRxiv*, 525014 (2019).

550 11. J. K. Mich, E. E. Hess, L. T. Graybuck, S. Somasundaram, J. A. Miller, Y. Ding, N. V.
551 Shapovalova, O. Fong, S. Yao, M. Mortrud, P. Chong, D. Bertagnolli, J. Goldy, T. Casper,
552 M. Kroll, R. D. Hodge, T. E. Bakken, Z. Yao, N. Dee, A. Cetin, K. A. Smith, R. P. Gwinn,
553 C. Cobbs, A. L. Ko, J. G. Ojemann, C. D. Keene, D. L. Silbergeld, V. Gradinaru, S. M.
554 Sunkin, H. Zeng, E. S. Lein, B. Tasic, J. T. Ting, B. P. Levi, Epigenetic landscape and
555 AAV targeting of human neocortical cell classes. *bioRxiv*, 555318 (2019).

556 12. A. Kepecs, G. Fishell, Interneuron cell types are fit to function. *Nature*. **505**, 318–326
557 (2014).

558 13. O. Marín, Interneuron dysfunction in psychiatric disorders. *Nat. Rev. Neurosci.* **13**, 107–120
559 (2012).

560 14. B. Rudy, G. Fishell, S. Lee, J. Hjerling-Leffler, Three groups of interneurons account for
561 nearly 100% of neocortical GABAergic neurons. *Dev. Neurobiol.* **71**, 45–61 (2011).

562 15. W. Muñoz, R. Tremblay, D. Levenstein, B. Rudy, Layer-specific modulation of neocortical
563 dendritic inhibition during active wakefulness. *Science*. **355**, 954–959 (2017).

564 16. X. Jiang, S. Shen, C. R. Cadwell, P. Berens, F. Sinz, A. S. Ecker, S. Patel, A. S. Tolias,
565 Principles of connectivity among morphologically defined cell types in adult neocortex.
566 *Science*. **350**, aac9462 (2015).

567 17. A. Melnikov, A. Murugan, X. Zhang, T. Tesileanu, L. Wang, P. Rogov, S. Feizi, A. Gnirke,
568 C. G. Callan, J. B. Kinney, M. Kellis, E. S. Lander, T. S. Mikkelsen, Systematic dissection
569 and optimization of inducible enhancers in human cells using a massively parallel reporter
570 assay. *Nat. Biotechnol.* **30**, 271–277 (2012).

571 18. D. Hartl, A. R. Krebs, J. Jüttner, B. Roska, D. Schübeler, Cis-regulatory landscapes of four
572 cell types of the retina. *Nucleic Acids Res.* **45**, 11607–11621 (2017).

573 19. S. Q. Shen, C. A. Myers, A. E. O. Hughes, L. C. Byrne, J. G. Flannery, J. C. Corbo,
574 Massively parallel cis-regulatory analysis in the mammalian central nervous system.
575 *Genome Res.* **26**, 238–255 (2016).

576 20. F. Inoue, M. Kircher, B. Martin, G. M. Cooper, D. M. Witten, M. T. McManus, N. Ahituv, J.
577 Shendure, A systematic comparison reveals substantial differences in chromosomal versus
578 episomal encoding of enhancer activity. *Genome Res.* **27**, 38–52 (2017).

579 21. M. Murtha, Z. Tokcaer-Keskin, Z. Tang, F. Strino, X. Chen, Y. Wang, X. Xi, C. Basilico, S.
580 Brown, R. Bonneau, Y. Kluger, L. Dailey, FIREWACh: High-throughput Functional
581 Detection of Transcriptional Regulatory Modules in Mammalian Cells. *Nat. Methods*. **11**,
582 559–565 (2014).

583 22. R. P. Patwardhan, J. B. Hiatt, D. M. Witten, M. J. Kim, R. P. Smith, D. May, C. Lee, J. M.
584 Andrie, S.-I. Lee, G. M. Cooper, N. Ahituv, L. A. Pennacchio, J. Shendure, Massively
585 parallel functional dissection of mammalian enhancers in vivo. *Nat. Biotechnol.* **30**, 265–
586 270 (2012).

587 23. A. M. Klein, L. Mazutis, I. Akartuna, N. Tallapragada, A. Veres, V. Li, L. Peshkin, D. A.
588 Weitz, M. W. Kirschner, Droplet Barcoding for Single-Cell Transcriptomics Applied to
589 Embryonic Stem Cells. *Cell*. **161**, 1187–1201 (2015).

590 24. E. Z. Macosko, A. Basu, R. Satija, J. Nemesh, K. Shekhar, M. Goldman, I. Tirosh, A. R.
591 Bialas, N. Kamitaki, E. M. Martersteck, J. J. Trombetta, D. A. Weitz, J. R. Sanes, A. K.
592 Shalek, A. Regev, S. A. McCarroll, Highly Parallel Genome-wide Expression Profiling of
593 Individual Cells Using Nanoliter Droplets. *Cell*. **161**, 1202–1214 (2015).

594 25. B. Tasic, V. Menon, T. N. Nguyen, T. K. Kim, T. Jarsky, Z. Yao, B. Levi, L. T. Gray, S. A.
595 Sorensen, T. Dolbeare, D. Bertagnolli, J. Goldy, N. Shapovalova, S. Parry, C. Lee, K.
596 Smith, A. Bernard, L. Madisen, S. M. Sunkin, M. Hawrylycz, C. Koch, H. Zeng, Adult
597 mouse cortical cell taxonomy revealed by single cell transcriptomics. *Nat. Neurosci.* **19**,
598 335–346 (2016).

599 26. S. Hrvatin, D. R. Hochbaum, M. A. Nagy, M. Cicconet, K. Robertson, L. Cheadle, R.
600 Zilionis, A. Ratner, R. Borges-Monroy, A. M. Klein, B. L. Sabatini, M. E. Greenberg,
601 Single-cell analysis of experience-dependent transcriptomic states in the mouse visual
602 cortex. *Nat. Neurosci.* **21**, 120–129 (2018).

603 27. H. Stroud, S. C. Su, S. Hrvatin, A. W. Greben, W. Renthal, L. D. Boxer, M. A. Nagy, D. R.
604 Hochbaum, B. Kinde, H. W. Gabel, M. E. Greenberg, Early-Life Gene Expression in
605 Neurons Modulates Lasting Epigenetic States. *Cell*. **171**, 1151-1164.e16 (2017).

606 28. C. N. Cearley, J. H. Wolfe, Transduction characteristics of adeno-associated virus vectors
607 expressing cap serotypes 7, 8, 9, and Rh10 in the mouse brain. *Mol. Ther. J. Am. Soc. Gene*
608 *Ther.* **13**, 528–537 (2006).

609 29. R. Zilionis, J. Nainys, A. Veres, V. Savova, D. Zemmour, A. M. Klein, L. Mazutis, Single-
610 cell barcoding and sequencing using droplet microfluidics. *Nat. Protoc.* **12**, 44–73 (2017).

611 30. J. Urban-Ciecko, A. L. Barth, Somatostatin-expressing neurons in cortical networks. *Nat.*
612 *Rev. Neurosci.* **17**, 401–409 (2016).

613 31. Y. Ma, H. Hu, A. S. Berrebi, P. H. Mathers, A. Agmon, Distinct subtypes of somatostatin-
614 containing neocortical interneurons revealed in transgenic mice. *J. Neurosci. Off. J. Soc.*
615 *Neurosci.* **26**, 5069–5082 (2006).

616 32. R. Tremblay, S. Lee, B. Rudy, GABAergic Interneurons in the Neocortex: From Cellular
617 Properties to Circuits. *Neuron*. **91**, 260–292 (2016).

618 33. H. Xu, H.-Y. Jeong, R. Tremblay, B. Rudy, Neocortical somatostatin-expressing GABAergic
619 interneurons disinhibit the thalamorecipient layer 4. *Neuron*. **77**, 155–167 (2013).

620 34. B. P. Bean, The action potential in mammalian central neurons. *Nat. Rev. Neurosci.* **8**, 451–
621 465 (2007).

622 35. T. Kimm, Z. M. Khaliq, B. P. Bean, Differential Regulation of Action Potential Shape and
623 Burst-Frequency Firing by BK and Kv2 Channels in Substantia Nigra Dopaminergic
624 Neurons. *J. Neurosci. Off. J. Soc. Neurosci.* **35**, 16404–16417 (2015).

625 36. B. N. Armbruster, X. Li, M. H. Pausch, S. Herlitze, B. L. Roth, Evolving the lock to fit the
626 key to create a family of G protein-coupled receptors potently activated by an inert ligand.
627 *Proc. Natl. Acad. Sci.* **104**, 5163–5168 (2007).

628